

1 **Shock-induced incongruent melting of olivine in Kamargaon L6**
2 **chondrite**

3 **Kishan Tiwari^{1,*}, Sujoy Ghosh¹, Masaaki Miyahara², Dwijesh Ray³**

4
5 ¹Department of Geology and Geophysics, Indian Institute of Technology, Kharagpur - 721302,
6 India

7 ²Graduate School of Advanced Science and Engineering, Hiroshima University, Higashi-
8 Hiroshima, Hiroshima 739-8526, Japan

9 ³Planetary Sciences Division, Physical Research Laboratory, Ahmedabad – 380009, India

10
11 Corresponding author: kishantiwari@iitkgp.ac.in
12
13

14 **Key Points:**

- 15 • We report shock-induced incongruent melting of olivine in an ordinary chondrite for
16 the first-time
- 17 • Olivine first dissociated to magnesiowüstite and liquid followed by crystallization of
18 bridgmanite from the residual liquid
- 19 • Olivine grains may have experienced pressure and temperature of ~25 GPa and
20 ~2500 °C
- 21
22
23
24
25

26 **Abstract**

27 Here we report for the first-time shock-induced incongruent melting of olivine in an
28 ordinary chondrite. Several olivine grains (Fo₇₄), entrained in the shock-melt vein of the
29 Kamargaon L6 chondrite were dissociated into magnesiowüstite ($X_{\text{Fe}} = 0.71$) and
30 orthoenstatite ($X_{\text{Fe}} = 0.22$). We propose that the breakdown of olivine took place as a result
31 of incongruent melting to produce magnesiowüstite and Mg-rich liquid. We suggest that
32 bridgmanite may have crystallized as the second phase from the olivine melt which back
33 transformed to a low-pressure phase of orthoenstatite from subsequent high-temperature and
34 low-pressure events. In this case, olivine grains may have experienced pressure and
35 temperature of ~25 GPa and ~2500 °C, respectively. Our results suggest that the incongruent
36 melting of olivine may possibly operate as one of the alternative mechanisms of dissociation
37 reaction driving the phase transformation of olivine in the natural systems.

38 **Plain language summary**

39 The planet Earth was formed from the similar material that constitutes present-day
40 asteroids which is mostly made up of olivine. Therefore, it is important to study olivine at
41 high pressure and high temperature to understand its behavior. Olivine breaks down into
42 bridgmanite and magnesiowüstite in the Earth's lower mantle which is one of the most
43 important reactions that largely controls the physical and chemical properties of the Earth's
44 interior. This breakdown may occur where the olivine remains in the solid-state or may also
45 form by melting of the olivine. The breakdown assemblage of bridgmanite and
46 magnesiowüstite formed by both of these mechanisms and has been reported in few Martian
47 meteorites. Recently, this breakdown assemblage by the solid-state has been reported in the
48 Suizhou meteorite. However, no such assemblage formed by melting has been found in
49 meteorites originated from the asteroid belt. We, for the first time, report the possible

50 occurrence of bridgmanite and magnesiowüstite formed by incongruent melting of olivine in
51 an ordinary chondrite. This assemblage may have formed at pressure and temperature of ~25
52 GPa and ~2500 °C. These observations suggest that the dissociation of olivine in the natural
53 systems can also take place by the melting of olivine.

54

55

56 **1. Introduction**

57 Olivine is volumetrically the most important phase of the Earth's upper mantle,
58 that undergoes successive pressure-dependent solid-state transformations to wadsleyite
59 (modified spinel structure) at 410-km and then to ringwoodite (spinel structure) at 520-km
60 ([Ringwoodite, 1991](#); [Frost, 2008](#)) and ultimately breaks down to form bridgmanite plus
61 magnesiowüstite at 660-km ([Ito & Takahashi, 1989](#)). In addition, high-pressure experiments
62 suggest that olivine melts incongruently into magnesiowüstite and liquid at above 8 GPa and
63 2100 °C ([Presnall & Walter, 1993](#); [Kato et al., 1998](#); [Ohtani et al., 1998](#)) because a
64 compositionally equivalent mixture of magnesiowüstite and liquid has lower free energy than
65 olivine melt at high-pressures ([Matsui & Kawamura, 1980](#); [Syono et al., 1981](#)). Therefore,
66 the dissociation mechanism of olivine is pivotal to understand the dynamics of the interior of
67 the Earth and other terrestrial planets because it affects the physical and chemical properties
68 such as densities and elastic velocities of mantle materials.

69 In addition to occurring in the Earth's interior, high pressure phase transformations,
70 dissociation reactions, and melting textures also occur as shock-induced features that are
71 primarily driven by high pressure and high temperature (HP-HT) conditions produced via
72 high-velocity collisions among asteroid parent bodies and impact events on the Moon and
73 Mars. Most of the high-pressure phases in shocked meteorites occur in and around shock-
74 induced melt veins (SMVs) (e.g., [Tomioka & Miyahara, 2017](#); [Miyahara et al., 2020](#)). The
75 solid-state polymorphic transformation of olivine to wadsleyite and ringwoodite have been
76 reported in chondrites ([Binns et al., 1969](#); [Ohtani et al., 2004](#); [Xie & Sharp, 2007](#); [Weisberg
77 & Kimura, 2010](#); [Miyahara et al., 2010](#)), Martian meteorites ([Greshake et al., 2013](#); [Walton et
78 al., 2014](#); [Miyahara et al., 2016](#); [Takenouchi et al., 2018](#)) and lunar meteorites ([Barrat et al.,
79 2005](#); [Zhang et al., 2010](#)). In contrast, olivine grains in contact with the matrix of melt veins
80 and melt pockets of shocked shergottites (DaG 735 and Tissint) have been dissociated to

81 vitrified bridgmanite + ferropericlae (Miyahara et al., 2011, 2016; Walton et al.,
82 2014). Recently, Bindi et al. (2020) reported dissociation of Fe-rich olivine ($X_{\text{Fe}} = 0.52$) to
83 hiroseite (Fe-rich bridgmanite, $X_{\text{Fe}} = 0.59$) and ferropericlae ($X_{\text{Fe}} = 0.44$) by the solid-state
84 transformation in the Suizhou L6 chondrite. However, natural dissociation of olivine by
85 incongruent melting has, to date, not been observed in shocked ordinary chondrites.

86 The Kamargaon meteorite fell on 13th November, 2015 near the town of Kamargaon,
87 which is located 27 km away from the Golaghat district of Assam, India (Goswami et al.,
88 2016) and was classified as an L6 chondrite (Ray et al., 2017). Previous studies on
89 Kamargaon L6 chondrite described olivine, pyroxene, plagioclase, and metal-sulfide
90 (kamacite, taenite, and troilite) as major rock-forming minerals, whereas chromite as an
91 accessory phase in the chondritic portion (Goswami et al., 2016; Ray et al., 2017). Ray et al.
92 (2017) calculated U-Th-⁴He, and K-Ar radiometric ages as 170 ± 25 and 684 ± 93 Ma and
93 cosmic ray exposure age as ~ 7 Ma for Kamargaon L6 chondrite. They observed shock
94 features like presence of mosaicism in olivine and pyroxene grains and maskelynite in the
95 host rock portion, formation of SMVs, polycrystalline troilite and metal-sulfide quenched
96 melt and accordingly suggested that the Kamargaon meteorite has experienced shock stage of
97 up to S5. The mineralogical and textural analysis of SMVs of Kamargaon L6 chondrite has
98 not been studied yet. In the present study, we carefully examined SMV present in the
99 Kamargaon L6 chondrite to understand dissociation and melting textures displayed by olivine
100 grains and their formation mechanisms which further provide clues to estimate the shock
101 conditions in the chondrite parent body.

102

103 **2. Materials and methods**

104 A small piece (~ 2 g) of Kamargaon chondrite was embedded in a low-viscosity epoxy
105 resin and its surface was polished using diamond paste. Preliminary textural observation and

106 phase identification was done using a scanning electron microscope (SEM) JEOL JSM-6490
107 installed at Indian Institute of Technology (IIT) Kharagpur, equipped with an energy-
108 dispersive spectrometer (EDS) operating at an acceleration voltage of 15 kV. The fine
109 textural variations and associations of different phases were investigated using a field
110 emission gun scanning electron microscope (FEG-SEM) using a JEOL JSM-7000F at
111 Tohoku University, with an acceleration voltage of 15 kV.

112 The chemical compositions of the various phases observed in Kamargaon L6
113 chondrite were obtained by electron probe microanalyser (EPMA) using a Cameca-SX 100
114 with three wavelength dispersive spectrometers (WDS) operating at an accelerating potential
115 of 15kV at Physical Research Laboratory (PRL), Ahmedabad. To minimize the beam damage
116 and loss of alkali elements, we analysed feldspar grains with the beam current and probe
117 diameter of 10 nA and 5 μm , respectively, whereas all the other phases were analysed with a
118 beam current of 15 nA and minimum beam diameter ($\sim 1 \mu\text{m}$). Minimum counting times were
119 20s on the peak and 10s on each side of the background. The following natural silicates,
120 sulfides and metal standards were used for calibration: diopside and plagioclase (Si), rutile
121 (Ti), kyanite (Al), wollastonite (Ca), almandine (Fe in silicates), iron metal (Fe in metal and
122 sulfide phase), olivine (Mg), rhodonite (Mn), jadeite (Na), orthoclase (K), apatite (P), pyrite
123 (S), chromite (Cr), nickel metal (Ni), cobalt metal (Co), vanadium metal (V). The data were
124 corrected for absorption, fluorescence, and atomic number effects using routine PAP (a Phi-
125 Rho-Z correction technique) procedure.

126 Different mineral phases and their polymorphs were identified using a laser micro-
127 Raman spectrometer, Horiba Jobin-Yvon LabRam HR800 at Indian Institute of Science
128 Education and Research (IISER) Kolkata, India. A microscope was used to focus the
129 excitation laser beam (a He-Ne laser, 633 nm line with 1800 L /mm grating). Laser power on

130 a sample was kept at 7.5 mW and the acquisition times were 10–30 s. For each phase, a
131 Raman shift was acquired in the spectral region of 200–1200 cm⁻¹.

132 Slice for TEM observations was prepared by a Focused Ion Beam (FIB) system using
133 a JEOL 9320-FIB at Tohoku University. A gallium ion beam was accelerated to 30 kV during
134 the sputtering of the slice, and the slice was approximately 100 nm in thickness. A JEOL
135 JEM-2100F field-emission (FE)-TEM operating at 200 kV with a JEOL energy-dispersive X-
136 ray spectroscopy (EDS) detector system was used for conventional TEM observation and
137 selected area electron diffraction (SAED) analyses at Tohoku University. We determined the
138 chemical composition of each mineral under the scanning TEM (STEM) mode with the EDS
139 detector. The chemical compositions were corrected using experimentally determined k-
140 factors [albite, pyrope, almandine, San Carlos olivine, and synthetic (Mg,Fe)O].

141 **3. Results**

142 The host rock of the Kamargaon L6 chondrite mainly consists of olivine (Fo₇₃₋₇₄),
143 low-calcium pyroxene (En₇₇₋₈₀Fs₁₉₋₂₂Wo₁₋₂), high-calcium pyroxene (En₄₅₋₄₆Fs₉₋₁₀Wo₄₄₋₄₆),
144 plagioclase (Ab₆₂₋₇₀An₁₈₋₂₃Or₁₂₋₁₅), Fe-Ni metal alloy (kamacite and taenite), troilite and a
145 minor amount of phosphate and chromite. The mid-portion of the sample consists of a major
146 thick SMV ranging in width from ~700 to 1600 μm. We observed that numerous olivine
147 grains entrained in the SMV have been dissociated into fine-grained granular assemblage.
148 The extent of dissociation of olivine grains seems to be dependent on the grain size and
149 location of grains in the SMV. The grains which are relatively coarser (>100 μm across)
150 and/or occur near the SMV-host rock boundary (vein edge) are partially dissociated and
151 exhibit heterogeneous texture and composition (Figs. 1a-b). Whereas the grains which are
152 finer (<100 μm across) and/or in the mid-portion of the SMV have been completely
153 dissociated (Fig. 1c). Partially dissociated olivine grains show dissociation texture as well as

154 vesicular texture and the core part of such grains displays vesicular texture. Whereas the
155 outer rim part of the grain exhibits dissociation texture. Spherulitic texture is common in
156 between them (Fig. 1b). The Raman spectra of these dissociated olivine grains exhibit two
157 strong peaks at ~821 (DB1) and ~853 (DB2) cm^{-1} corresponding to characteristic doublet
158 attributed to symmetric and asymmetric stretching vibrations of Si-O bond in SiO_4 tetrahedra
159 in olivine structure (McMillan & Akaogi, 1987) and apparently relatively a weak, less sharp
160 peak at ~664 cm^{-1} indicates the presence of pyroxene glass (Fig. 2) (Kubicki et al., 1992).
161 These measured Raman spectra were used to measure the composition of the residual olivine
162 that escaped the dissociation. The forsterite content of the residual olivine was established
163 using olivine of terrestrial, meteoritic and synthetic origin by combining the doublet (DB1
164 and DB2) peak positions (Kuebler et al., 2006):

$$165 \quad \text{Fo} = (80.19x_1 + 399.35x_2 - 0.04x_1^2 - 0.24x_2^2 - 206232.99) \times 100 \quad (1)$$

166 where Fo is forsterite content, x_1 and x_2 are peak positions of DB1 and DB2, respectively.
167 Using this relationship, calculated Fo content of the residual olivine in Kamargaon L6
168 chondrite is $\sim 75 \pm 10$. The Raman spectra of the olivine grains present in the host rock show a
169 strong doublet at peak positions of ~820.4 and ~851.4 cm^{-1} (Fig. 2). Their Fo contents
170 calculated from Eq. (1) of $\sim 75 \pm 10$ and match well with measured Fo content of the host
171 olivine grains of ~74 using electron probe micro analyzer (Table 1). This suggests that the
172 calculated Fo contents of dissociated olivine using Raman data is reliable for our sample.

173 A thin slice ($\sim 20 \times 7 \times 10 \mu\text{m}$) of a bean shaped ($\sim 92 \times 40 \mu\text{m}$) completely
174 dissociated olivine grain in the SMV, adjacent to the vein edge (Fig. 1c) was excavated by a
175 FIB system and analyzed using a TEM to further investigate the assemblage and
176 microtextures of dissociated olivine. A high angle annular dark field (HAADF) image of the
177 TEM slice and STEM EDS analysis exhibit micro porphyritic texture where bright euhedral

178 grains with (Mg,Fe)O composition are embedded in grey matrix consisting of (Mg,Fe)SiO₃
179 (Fig. 3a-b, Table 1). The selected area electron diffraction (SAED) patterns confirm that the
180 bright grains are magnesiowüstite indexed to cubic structure with $a = 4.38 \text{ \AA}$ (Fig. 3c) and the
181 grey matrix is orthorhombic enstatite (hereafter orthoenstatite) with $b = 10.3 \text{ \AA}$ (Fig. 3d). The
182 magnesiowüstites are dimensionally much larger (up to $\sim 500 \text{ nm}$ across) than the elongated
183 orthoenstatites ($\sim 50 \text{ nm} \times \sim 200 \text{ nm}$). The elongated microlites of orthoenstatite grains display
184 dendritic texture (Fig. 3b) which radiates perpendicularly outwards from individual
185 magnesiowüstites. TEM-EDS analyses shows that magnesiowüstite (Mg_{0.3}Fe_{0.7}O) have X_{Fe}
186 [molar Fe/(Fe+Mg)] of 0.71 whereas orthoenstatite (Mg_{1.85}Fe_{0.25}Si_{1.9}O₆) have X_{Fe} of 0.12
187 (Table 1).

188 4. Discussion

189 Dissociated assemblage of bridgmanite and magnesiowüstite in high-pressure
190 experiments (Frost & Langenhorst, 2002; Sinmyo et al., 2008) and Martian meteorites (DaG
191 735 and Tissint, Miyahara et al., 2011, 2016) shows equigranular texture with $\sim 120^\circ$ triple
192 junctions between coexisting bridgmanite and magnesiowüstite grain. These textures have
193 been interpreted to be the evidence of the solid-state transformation due to the simultaneous
194 and random nucleation as well as crystal growth of the coexisting phases. In contrast, a
195 dissociated assemblage of bridgmanite and magnesiowüstite resulting from incongruent
196 melting in high-pressure experiments (Kato et al., 1998; Ohtani et al., 1998) and Martian
197 meteorite (NWA 2737, Miyahara et al., 2019) displays normally euhedral to subhedral grains
198 of the first liquidus phase and finer grained subsequent second liquidus phase that occupy the
199 interstitial space.

200 Thus, incongruent melting of olivine results in porphyritic texture where the
201 dimensionally larger grains of phenocrysts are generally the first liquidus phase. Dissociated

202 olivines in the Kamargaon L6 chondrite show micro-porphyritic texture with no triple
203 junctions along the grain boundaries. Therefore, we propose that the dissociation assemblage
204 is as a result of the melting of olivine. We carefully examine the texture and Raman spectra
205 of the dissociated part of olivine to test two possibilities for the formation of orthoenstatite:
206 (1) crystallization of orthoenstatite directly from the melt, and (2) crystallization
207 of bridgmanite from the residual melt which was back-transformed to a low-pressure phase of
208 orthoenstatite as a result of subsequent high-temperature event.

209 To understand the first proposed scenario of crystallization of orthoenstatite directly
210 from the melt we consider the melting experiments in the Mg_2SiO_4 - Fe_2SiO_4 system which
211 have shown that the olivine (Fa_{10}) begins to melt incongruently above 8.5 GPa and 2050 °C
212 to magnesiowüstite and Mg-rich silicate liquid (Ohtani et al., 1998). It is likely that with
213 increasing pressure, the incongruent melting temperature of olivine increases but decreases
214 by the addition of fayalite component. We observed that the fayalite content of olivine
215 present in the host rock of Kamargaon is higher (Fa_{26}) than that of the synthetic olivine used
216 by Ohtani et al. (1998). Therefore, we infer that the olivine grains were partially or
217 completely melted incongruently to produce magnesiowüstite and melt, followed by
218 crystallization of orthoenstatite from the residual melt. These orthoenstatites may have
219 crystallized directly from the residual liquid during rapid cooling as indicated by their
220 dendritic texture. The heterogeneity in degree of incongruent melting may possibly be
221 because of the development of temperature gradient in the olivine grains entrained in SMVs
222 as their outer surface is in direct contact with shock melt which makes their inner core portion
223 relatively cooler.

224 Crystalline structure of natural bridgmanite ($X_{Mg} = 0.78$) has been reported to coexist
225 with akimotoite in shocked Tenham L6 chondrite (Tschauner et al., 2013). These fine-grained
226 polycrystalline bridgmanite are formed by the solid-state phase transformation from

227 orthoenstatite. Most of the crystalline bridgmanite reported in shocked meteorites are found
228 in vitrified state (Sharp et al., 1997; Tomioka & Fujino, 1997; Tomioka & Kimura, 2003;
229 Chen et al., 2004; Xie et al., 2006) due to the following reasons: (1) bridgmanite becomes
230 unstable at high post-shock temperature after decompression (Durben & Wolf, 1992; Kubicki
231 et al., 1992), (2) it may also get easily damaged by ion sputtering during FIB sample
232 preparation, and (3) under electron beam bombardment in TEM analysis (Sharp et al., 1997;
233 Tomioka & Fujino, 1997). In the present study, no such vitrified phase is observed in the
234 dissociated grains of olivine in Kamargaon. However, orthoenstatite coexisting with
235 magnesiowüstite is identified as a dissociation product of olivine. The Raman spectra from
236 the dissociated portion indicate the presence of pyroxene glass (Fig. 2) although we did not
237 find any vitrified phase with (Mg,Fe)SiO₃ composition in the part excavated for TEM
238 observation. Miyahara et al. (2011) observed a similar Raman peak at 665 cm⁻¹ from the
239 dissociated olivine in Martian meteorite (DaG 735) and interpreted that it corresponds to
240 vitrified bridgmanite. Thus, the Raman peak at 664 cm⁻¹ we observed from the dissociated
241 portion of shocked Kamargaon L6 chondrite might correspond to the remnant of vitrified
242 bridgmanite that was absent in the portion analyzed by TEM. Forsteritic olivine (Fa₁₀) melts
243 incongruently to magnesiowüstite and liquid at 23 GPa but the assemblage changes to
244 magnesiowüstite and bridgmanite at ~25 GPa and ~2500 °C (Ohtani et al., 1998). It is likely
245 that the incongruent melting of olivine took place at or above the pressure of 25 GPa and
246 magnesiowüstite and bridgmanite were crystallized as the dissociation product. In this case,
247 olivine grains may have experienced similar pressure and temperature of ~25 GPa and ~2500
248 °C, respectively.

249 We found that albitic feldspar (Ab₆₅An₂₁Or₁₄) grains in and around the SMV in
250 Kamargaon L6 chondrite has been transformed into maskelynite. Such transformation
251 requires pressure of ≥ 29-30 GPa (Fritz et al., 2011). This indicates that the pressure was

252 higher than 25 GPa required to produce bridgmanite and magnesiowüstite as the dissociation
253 product. Therefore, we suggest that the crystallization of bridgmanite as the second phase and
254 its subsequent back transformation to orthoenstatite is a more plausible scenario. It has been
255 previously suggested that shock induced melt produced in the SMVs can get superheated far
256 above their liquidus temperature (Sharp et al., 2015). We propose that Mg-rich liquid in the
257 incongruently melted olivine may have been superheated. The bridgmanite started
258 crystallizing from this Mg-rich liquid when the temperature was dropping rapidly but was
259 still above 2500 °C and thus producing a dendritic texture. The bridgmanite may have later
260 back-transformed to a low-pressure phase of orthoenstatite as a result of subsequent high
261 temperature and low-pressure event via a solid-state reaction. Such occurrence of back
262 transformed pyroxene and magnesiowüstite assemblage has been reported as inclusions in
263 sublithospheric diamonds (Hutchison et al., 2001; Zedgenizov et al., 2020). Therefore,
264 orthoenstatite may have retained the morphology of original ultra-fine elongated microlites of
265 bridgmanite. Also, it has been experimentally established that the melting temperature of
266 bridgmanite is lower than that of magnesiowüstite at lower pressures (Zerr & Boehler, 1994).
267 Therefore, alternatively, the subsequent high temperature and lower pressure event may have
268 partially melted the dissociated olivine grains where the bridgmanite occurring in the
269 interstitial space between the magnesiowüstite grains may have melted and crystallized as
270 low-pressure polymorph of orthoenstatite during rapid cooling. The estimated shock pressure
271 of ≥ 25 GPa for Kamargaon L6 chondrite is similar to the shock pressure of ~ 23 -26 GPa
272 estimated for other heavily shocked meteorites in which the bridgmanite has formed in the
273 SMVs (Sharp et al., 1997; Tomioka & Fujino, 1997; Tomioka & Kimura, 2003; Chen et al.,
274 2004; Xie et al., 2006; Miyahara et al., 2011).

275 We calculated the modal proportion of orthoenstatite and magnesiowüstite in the
276 Kamargaon L6 chondrite using the image analysis software (ImageJ) and estimated that the

277 ratio is 69:31 for orthoenstatite and magnesiowüstite which is very similar to the modal
278 proportion of bridgmanite and magnesiowüstite formed by the solid-state transformation in
279 high-pressure experiments and the Martian meteorite of DaG 735 (~70:30) (Ito & Takahashi,
280 1989; Miyahara et al., 2011). However, extra-terrestrial olivine studied here is slightly Fe-
281 rich (Fa₂₆) compared to olivine (Fa₈₋₁₂) from the upper mantle. In addition, dissociation
282 mechanism of Kamargaon olivine, i.e., incongruent melting, is different from the solid-state
283 dissociation mechanism of olivine expected in the Earth's mantle. However, natural evidence
284 of dissociation of olivine by incongruent melting to lower mantle assemblage presented in
285 this study and the resulting similar modal ratio of coexisting phases to that of the solid-state
286 dissociation compels us to consider incongruent melting of olivine as possibly one of the
287 alternative mechanisms driving the phase transformation of olivine in the natural systems if
288 provided with the sufficient pressure and temperature.

289

290 **5. Conclusions**

291 Here we report for the first-time shock-induced incongruent melting of olivine
292 dissociated into magnesiowüstite and orthoenstatite in an ordinary chondrite. Based on the
293 textural observations, we suggest that this dissociated assemblage formed by incongruent
294 melting of olivine into magnesiowüstite and Mg-rich melt in the shocked Kamargaon L6
295 chondrite.. We propose that the incongruent melting took place at or above the pressure and
296 temperature of ~25 GPa and ~2500 °C to produce magnesiowüstite and Mg-rich melt and
297 subsequently bridgmanite crystallized from the Mg-rich melt. The bridgmanite was heated
298 and back transformed to low pressure phase of orthoenstatite as a result of subsequent high-
299 temperature and low-pressure event. These observations point towards the possibility of
300 incongruent melting operating as an alternate mechanism for phase transformation in the
301 natural systems when subjected to sufficiently high-pressure and high-temperature condition.

302

303 **Acknowledgments**

304 S.G. acknowledges the financial support by Council of Scientific and Industrial Research
305 (CSIR) grant 24(0362)/20/EMR-II. K.T. acknowledges the support for his Ph.D. fellowship
306 from University Grants Commission, Government of India. We thank G. D. Mukherjee for
307 providing a laser micro-Raman facility at IISER Kolkata. Careful reviews by two anonymous
308 reviewers and editorial handling by Steve Jacobsen were greatly appreciated. All the data
309 used in this study, including all the figures (Fig. 1 to 3) and table (Table 1) in this manuscript,
310 can be accessed through the following DOI: <https://doi.org/10.6084/m9.figshare.14341772.v1>

311

312 **References**

- 313 Barrat, J. A., Chaussidon, M., Bohn, M., Gillet, P., Göpel, C., & Lesourd, M. (2005). Lithium
314 behavior during cooling of a dry basalt: An ion-microprobe study of the lunar meteorite
315 Northwest Africa 479 (NWA 479). *Geochimica et Cosmochimica Acta*, 69(23), 5597-
316 5609. DOI: 10.1016/j.gca.2005.06.032
- 317 Binns R. A., Davis R. J., & Reed S. J. B. (1969). Ringwoodite, natural (Mg,Fe)₂SiO₄ spinel
318 in the Tenham meteorite. *Nature*, 221, 943–944. DOI:10.1038/221943a0
- 319 Bindi, L., Shim, S. H., Sharp, T. G., & Xie, X. (2020). Evidence for the charge
320 disproportionation of iron in extraterrestrial bridgmanite. *Science advances*, 6(2),
321 eaay7893. DOI: 10.1126/sciadv.aay7893
- 322 Chen M., Xie, X. & Goresy, A. E. (2004). A shock-produced (Mg,Fe)SiO₃ glass in the
323 Suizhou meteorite. *Meteoritics and Planetary Science*, 39: 1797-1808.
324 DOI:10.1111/j.1945-5100.2004.tb00076.x
- 325 Durben, D. J., & Wolf, G. H. (1992). High-temperature behavior of metastable MgSiO₃
326 perovskite: a Raman spectroscopic study. *American Mineralogist*, 77(7-8), 890-893.
- 327 Fritz, J., Wünnemann, K., Greshake, A., Fernandes, V. A. S. M., Boettger, U., & Hornemann,
328 U. (2011). Shock pressure calibration for lunar plagioclase. *Lunar and planetary science*
329 *conference*, 42. Abstract #1196.
- 330 Frost, D.J. (2008) The upper mantle and transition zone. *Elements*, 4(3), pp.171-176.DOI:
331 10.2113/GSELEMENTS.4.3.171
- 332 Frost, D. J., & Langenhorst, F. (2002). The effect of Al₂O₃ on Fe–Mg partitioning between
333 magnesiowüstite and magnesium silicate perovskite. *Earth and Planetary Science*
334 *Letters*, 199(1-2), 227-241. DOI:10.1016/S0012-821X(02)00558-7

- 335 Goswami T.K., Ray D., Sarmah R.K., Goswami U., Bhattacharyya P., Majumdar D.,
336 Bezbaruah D., & Borgohain P. (2016). Meteorite fall at Komargaon, Assam, India.
337 *Current Science*, 110(10), 1894-1895.
- 338 Greshake A., Fritz J., Böttger U., & Goran D. (2013). Shear induced ringwoodite formation
339 in the Martian shergottite Dar al Gani 670. *Earth and Planetary Science Letters*,
340 375:383–394. DOI:10.1016/j.epsl.2013.06.002.
- 341 Hutchison, M. T., Hursthouse, M. B., & Light, M. E. (2001). Mineral inclusions in diamonds:
342 associations and chemical distinctions around the 670-km discontinuity. *Contributions to*
343 *Mineralogy and Petrology*, 142(1), 119-126. DOI:10.1007/s004100100279
- 344 Ito E. & Takahashi E. (1989). Post-spinel transformations in the system Mg_2SiO_4 - Fe_2SiO_4
345 and some geophysical implications. *Journal of Geophysical Research: Solid Earth*,
346 94:10637–10646. DOI:10.1029/JB094iB08p10637
- 347 Kato, T., Nakata, N., Ohtani, E., & Onuma, K. (1998). Melting experiments on the forsterite–
348 pyrope system at 8 and 13.5 GPa. *Physics of the earth and planetary interiors*, 107(1-3),
349 97-102. DOI:10.1016/S0031-9201(97)00127-1
- 350 Kubicki J. D., Hemley R. J., & Hofmeister, A. M. (1992). Raman and infrared study of
351 pressure-induced structural changes in $MgSiO_3$, $CaMgSi_2O_6$, and $CaSiO_3$ glasses.
352 *American Mineralogist*, 77(3-4), 258-269.
- 353 Kuebler K. E., Jolliff B. L., Wang A., & Haskin L. A. (2006). Extracting olivine (Fo-Fa)
354 compositions from Raman spectral peak positions. *Geochimica et Cosmochimica Acta*,
355 70:6201–6222. DOI:10.1016/j.gca.2006.07.035
- 356 Matsui, Y., & Kawamura, K. (1980). Instantaneous structure of an $MgSiO_3$ melt simulated by
357 molecular dynamics. *Nature*, 285, 648-649. DOI:10.1038/285648a0
- 358 McMillan, P. F., & Akaogi, M. (1987). Raman spectra of beta- Mg_2SiO_4 (modified spinel) and
359 gamma- Mg_2SiO_4 (spinel). *American Mineralogist*, 72(3-4), 361-364.
- 360 Miyahara M., Ohtani E., El Goresy A., Ozawa S., & Gillet P. (2016). Phase transition
361 processes of olivine in the shocked Martian meteorite Tissint: Clues to origin of
362 ringwoodite-, bridgmanite- and magnesiowüstite-bearing assemblages. *Physics of the*
363 *earth and planetary interiors*, 259:18–28. DOI:10.1016/j.pepi.2016.08.006
- 364 Miyahara M., Ohtani E., Kimura M., El Goresy A., Ozawa S., Nagase T., Nishijima M., &
365 Hiraga K. (2010). Coherent and subsequent incoherent ringwoodite growth in olivine of
366 shocked L6 chondrites. *Earth and Planetary Science Letters*, 295:321–327.
367 DOI:10.1016/j.epsl.2010.04.023
- 368 Miyahara, M., Ohtani, E., Nishijima, M., & El Goresy, A. (2019). Olivine melting at high
369 pressure condition in the chassignite Northwest Africa 2737. *Physics of the earth and*
370 *planetary interiors*, 291, 1-11. DOI:10.1016/j.pepi.2019.04.001
- 371 Miyahara, M., Ohtani, E., Ozawa, S., Kimura, M., El Goresy, A., Sakai, T., Nagase, T.,
372 Hiraga, K., Hirao, N. & Ohishi, Y. (2011). Natural dissociation of olivine to $(Mg,Fe)SiO_3$
373 perovskite and magnesiowüstite in a shocked Martian meteorite. *Proceedings of the*
374 *National Academy of Sciences*, 108(15), pp.5999-6003. DOI:10.1073/pnas.1016921108

375 Miyahara, M., Yamaguchi, A., Saitoh, M., Fukimoto, K., Sakai, T., Ohfuji, H., Tomioka, N.,
376 Kodama, Y., & Ohtani, E. (2020). Systematic investigations of high-pressure polymorphs
377 in shocked ordinary chondrites. *Meteoritics and Planetary Science*, 55, 2619-2651. DOI:
378 10.1111/maps.13608

379 Ohtani, E., Moriwaki, K., Kato, T., & Onuma, K. (1998). Melting and crystal–liquid
380 partitioning in the system Mg_2SiO_4 – Fe_2SiO_4 to 25 GPa. *Physics of the earth and*
381 *planetary interiors*, 107(1-3), 75-82. DOI:10.1016/S0031-9201(97)00125-8

382 Ohtani, E., Kimura, Y., Kimura, M., Takata, T., Kondo, T., & Kubo, T. (2004). Formation of
383 high-pressure minerals in shocked L6 chondrite Yamato 791384: constraints on shock
384 conditions and parent body size. *Earth and Planetary Science Letters*, 227(3-4), 505-515.
385 DOI:10.1016/j.epsl.2004.08.018

386 Presnall, D. C., & Gasparik, T. (1990). Melting of enstatite ($MgSiO_3$) from 10 to 16.5 GPa
387 and the forsterite (Mg_2SiO_4)-majorite ($MgSiO_3$) eutectic at 16.5 GPa: Implications for the
388 origin of the mantle. *Journal of Geophysical Research: Solid Earth*, 95(B10), 15771-
389 15777. DOI:10.1029/JB095iB10p15771

390 Presnall, D. C., & Walter, M. J. (1993). Melting of forsterite, Mg_2SiO_4 , from 9.7 to 16.5 GPa.
391 *Journal of Geophysical Research: Solid Earth*, 98(B11), 19777-19783. DOI:
392 10.1029/93JB01007

393 Ray D., Mahajan, R. R., Shukla, A. D., Goswami, T. K., & Chakraborty, S. (2017).
394 Petrography, classification, oxygen isotopes, noble gases, and cosmogenic records of
395 Kamargaon (L6) meteorite: The latest fall in India. *Meteoritics and Planetary Science*,
396 52(8), 1744-1753. DOI:10.1111/maps.12875

397 Ringwood, A. E. (1991). Phase transformations and their bearing on the constitution and
398 dynamics of the mantle. *Geochimica et Cosmochimica Acta*, 55(8), 2083-2110.
399 DOI:10.1016/0016-7037(91)90090-R

400 Sharp T.G., Lingemann C.M., Dupas C. & Stöffler D. (1997), Natural occurrence of $MgSiO_3$ -
401 ilmenite and evidence for $MgSiO_3$ -perovskite in a shocked L chondrite. *Science*, 277,
402 352–355. DOI: 10.1126/science.277.5324.352

403 Sharp, T. G., Xie, Z., de Carli, P. S., & Hu, J. (2015). A large shock vein in L chondrite
404 Roosevelt County 106: Evidence for a long-duration shock pulse on the L chondrite
405 parent body. *Meteoritics & Planetary Science*, 50(11), 1941-1953.
406 DOI:10.1111/maps.12557

407 Sinmyo, R., Hirose, K., Nishio-Hamane, D., Seto, Y., Fujino, K., Sata, N., & Ohishi, Y.
408 (2008). Partitioning of iron between perovskite/postperovskite and ferropericlaase in the
409 lower mantle. *Journal of Geophysical Research: Solid Earth*, 113(B11).
410 DOI:10.1029/2008JB005730

411 Syono, Y., Goto, T., Takei, H., Tokonami, M., & Nobugai, K. (1981). Dissociation reaction
412 in forsterite under shock compression. *Science*, 214(4517), 177-179.
413 DOI:10.1126/science.214.4517.177

414 Takenouchi, A., Mikouchi, T., & Yamaguchi, A. (2018). Shock veins and brown olivine in
415 Martian meteorites: Implications for their shock pressure–temperature histories.
416 *Meteoritics & Planetary Science*, 53, 2259–2284. DOI: 10.1111/maps.13120

417 Tomioka N. and Miyahara, M. (2017). High-pressure minerals in shocked meteorites.
418 *Meteoritics and Planetary Science*, 52, 2017-2039. DOI:10.1111/maps.12902

419 Tomioka N. and Kimura, M. (2003). The breakdown of diopside to Ca-rich majorite and
420 glass in a shocked H chondrite. *Earth and Planetary Science Letters*, 208(3-4), pp.271-
421 278. DOI:10.1016/S0012-821X(03)00049-9

422 Tomioka, N. & Fujino, K. (1997). Natural (Mg,Fe)SiO₃-ilmenite and-perovskite in the
423 Tenham meteorite. *Science*, 277, 1084-1086. DOI: 10.1126/science.277.5329.1084

424 Tschauner, O., Ma, C., Beckett, J. R., Prescher, C., Prakapenka, V. B., & Rossman, G. R.
425 (2014). Discovery of bridgmanite, the most abundant mineral in Earth, in a shocked
426 meteorite. *Science*, 346(6213), 1100-1102. DOI: 10.1126/science.1259369

427 Walton E. L., Sharp T. G., & Hu J. (2014). Heterogeneous mineral assemblages in Martian
428 meteorite Tissint as a result of a recent small impact event on Mars. *Geochimica et*
429 *Cosmochimica Acta*, 140:334–348. DOI:10.1016/j.gca.2014.05.023

430 Weisberg M. K. & Kimura M. (2010). Petrology and Raman spectroscopy of high pressure
431 phases in the Gujba CB chondrite and the shock history of the CB parent body.
432 *Meteoritics and Planetary Science*, 45:873–884. DOI:10.1111/j.1945-
433 5100.2010.01058.x

434 Xie Z. & Sharp T. G. (2007). Host rock solid-state transformation in a shock-induced melt
435 vein of Tenham L6 chondrite. *Earth and Planetary Science Letters*, 254:433–445.
436 DOI:10.1016/j.epsl.2006.12.001

437 Xie Z., Sharp T. G., and DeCarli P. S. (2006). High-pressure phases in a shock-induced melt
438 vein of the Tenham L6 chondrite: Constraints on shock pressure and duration.
439 *Geochimica et Cosmochimica Acta*, 70:504–515. DOI:10.1016/j.gca.2005.09.003

440 Zedgenizov, D., Kagi, H., Ohtani, E., Tsujimori, T., & Komatsu, K. (2020). Retrograde
441 phases of former bridgmanite inclusions in superdeep diamonds. *Lithos*, 370, 105659.
442 DOI:10.1016/j.lithos.2020.105659

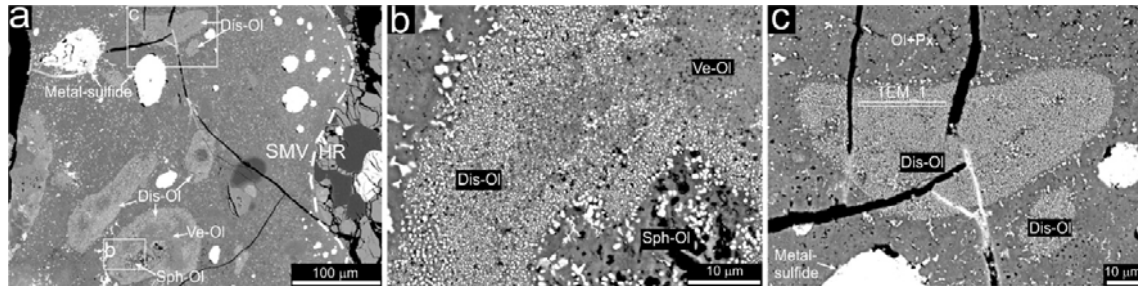
443 Zerr, A., & Boehler, R. (1994). Constraints on the melting temperature of the lower mantle
444 from high-pressure experiments on MgO and magnesiowüstite. *Nature*, 371(6497), 506-
445 508. DOI:10.1038/371506a0

446 Zhang A., Hsu W., Floss C., Li X., Li Q., Liu Y., & Taylor L. A. (2010). Petrogenesis of
447 lunar meteorite Northwest Africa 2977: Constraints from in situ microprobe results.
448 *Meteoritics and Planetary Science*, 45:1929–1947. DOI:10.1111/j.1945-
449 5100.2010.01131.x

450

451 **Figures**

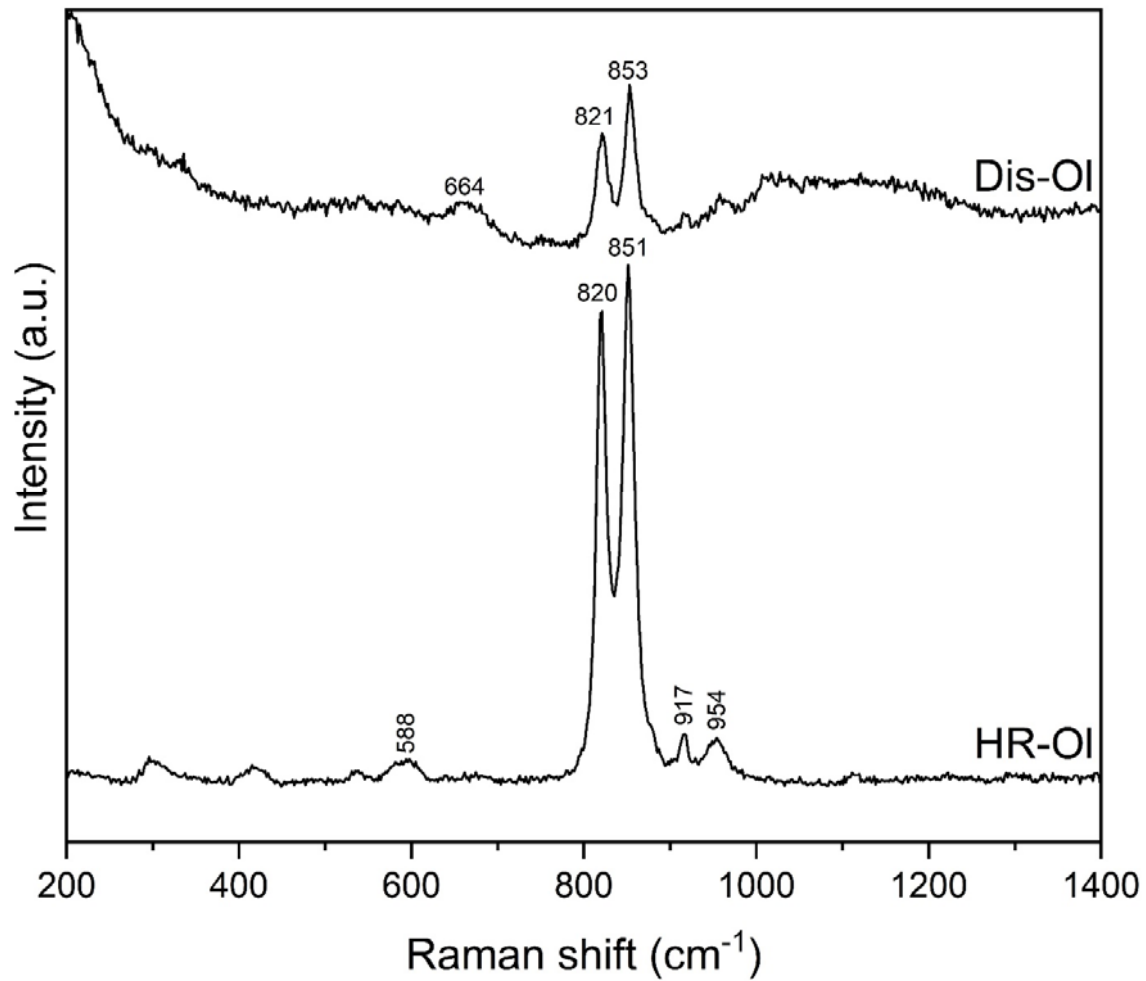
452



453

454 **Figure 1 (a)** Low magnification back-scattered electron image of the portion of SMV of
455 Kamargaon L6 chondrite shows various completely and partially dissociated olivine grains
456 and metal-sulfide spherules. **(b)** High magnification image of the boxed area in Fig. 1a
457 labelled as b, shows part of the partially dissociated olivine grain. The rim portion of the
458 grains have been dissociated whereas the core portion is vesicular and spherulitic texture.
459 Such heterogeneous texture mainly depicts the formation of temperature gradient in olivine
460 grains entrained in the hot melt vein. **(c)** High magnification image of the boxed area in Fig.
461 1a labelled as c, shows relatively finer grains which have been completely dissociated. The
462 portions marked as TEM_1 was excavated by using FIB for the TEM analysis. Ve-Ol =
463 vesicular olivine; Dis-Ol = dissociated olivine; Sph-Ol = spherulitic olivine; Ol+Px = olivine
464 + pyroxene assemblage; SMV = shock-melt vein; HR = host rock.

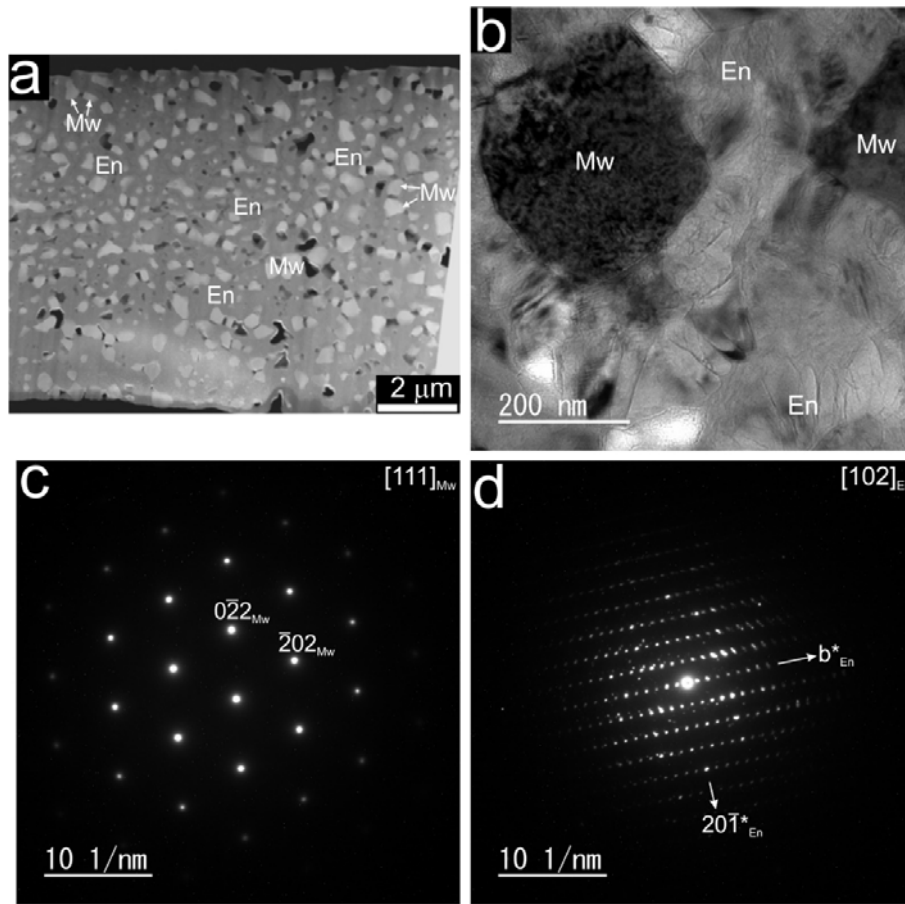
465



466

467 **Figure 2** Representative Raman spectra of dissociated (Dis-Ol) and host rock olivine (HR-
 468 Ol). Raman analysis of the HR-Ol produces intense doublets at ~820 and ~851 cm⁻¹ whereas
 469 the Raman spectra of Dis-Ol grains display two strong peaks at ~821 (DB1) and ~853 (DB2)
 470 cm⁻¹ apparently relatively a weak. Less sharp peak at ~664 cm⁻¹ indicates the presence of
 471 pyroxene glass.

472



473

474 **Figure 3 (a)** High-angle annular dark field (HAADF) image of the slice cut from the portion
 475 marked in Fig. 1c shows micro-porphyritic texture where bright relatively coarser grained
 476 magnesiowüstite is set in a grey matrix of finer grained orthoenstatite. **(b)** Bright-field TEM
 477 image shows the fine textures of dissociated olivine. Fine elongated microlites of
 478 orthoenstatite consist the grey matrix in which the coarse magnesiowüstite grains are set. **(c)**
 479 and **(d)** are electron diffraction patterns of magnesiowüstite and orthoenstatite respectively.

480 Mw = magnesiowüstite; En = orthoenstatite.

481

482

483 **Table 1** Chemical composition (in wt. %) of olivine present in the host rock analyzed by EPMA
 484 and orthoenstatite and magnesiowüstite formed from dissociated olivine in shock melt vein of
 485 the Kamargaon L6 chondrite analyzed by STEM-EDS.

	EPMA		STEM-EDS [#]			
Location	HR-Ol		Dis-Ol			
Phases	Ol	1 σ	Oen	1 σ	Mw	1 σ
n	21		12		7	
SiO ₂	37.48	0.47	55.40	1.77	1.55	0.35
FeO*	24.44	0.24	8.51	0.81	80.44	1.09
MnO	0.45	0.04	n.d.	n.d.	n.d.	n.d.
MgO	38.01	0.16	36.09	1.64	18.01	1.19
CaO	0.04	0.03	n.d.	n.d.	n.d.	n.d.
Total	100.42		100		100	
Cation						
Si	0.978	0.009	1.906	0.072	0.016	0.004
Fe ²⁺	0.533	0.006	0.245	0.024	0.280	0.016
Mn	0.010	0.001	-	-	-	-
Mg	1.478	0.007	1.849	0.071	0.703	0.015
Ca	0.001	0.001	-	-	-	-
Oxygen	4		6		1	
Fa	26					
X _{Fe} × 100			12		71	

486

487 Fa = fayalite content, X_{Fe} = Fe/(Mg+Fe); Oen = orthoenstatite, Mw = magnesiowüstite; Dis-Ol
 488 = dissociated olivine; HR-Ol = host rock olivine; # = Total is normalized to 100 %; * = All
 489 iron is assumed to be ferrous, n = number of analyses; 1 σ = standard deviation, n.d. = not
 490 determined.